# Tunable Cr4+ molecular color centers

Daniel W. Laorenza,<sup>1,2</sup> Arailym Kairalapova,<sup>3</sup> Sam L. Bayliss,<sup>4</sup> Tamar Goldzak,<sup>3</sup> Samuel M. Greene,<sup>3</sup> Leah R. Weiss,<sup>4</sup> Pratiti Deb,<sup>4,5</sup> Peter J. Mintun,<sup>4</sup> Kelsey A. Collins,<sup>2</sup> David D. Awschalom,\*,<sup>4,5,6</sup> Timothy C. Berkelbach,\*,<sup>3,7</sup> and Danna E. Freedman\*,<sup>1,2</sup>

- 1 Department of Chemistry, Massachusetts Institute of Technology, Cambridge, Massachusetts 02139, United States.
- 2 Department of Chemistry, Northwestern University, Evanston, Illinois 60208, United States.
- 3 Department of Chemistry, Columbia University, New York, New York 10027, United States.
- 4 Pritzker School of Molecular Engineering, University of Chicago, Chicago, IL 60637, USA.
- 5 Department of Physics, University of Chicago, Chicago, IL 60637, USA.
- 6 Center for Molecular Engineering and Materials Science Division, Argonne National Laboratory, Lemont, IL 60439, USA.
- $7\ Center\ for\ Computational\ Quantum\ Physics, Flatiron\ Institute, New\ York, New\ York\ 10010, United\ States.$

**ABSTRACT:** The inherent atomistic precision of synthetic chemistry enables bottom-up structural control over quantum bits, or qubits, for quantum technologies. Tuning paramagnetic molecular qubits that feature optical spin initialization and readout is a crucial step towards designing bespoke qubits for applications in quantum sensing, networking, and computing. Here, we demonstrate that the electronic structure that enables optical spin initialization and readout for S = 1,  $Cr(aryl)_4$ , where aryl = 2, 4-dimethylphenyl (1), 4, 4-dimethylphenyl (2), 4-dimethylphenyl (3), is readily translated into 4-dimethylphenyl (4), 4-dimethylsilyl)methyl (5), and cyclohexyl (6). The small ground-state zero field splitting values (4-dimethylphenyl (5), and cyclohexyl (6). The small ground-state zero field splitting values (4-dimethylphenyl (7), 4-dimethylsilyl)methyl (8), and cyclohexyl (9). The small ground-state zero field splitting values (4-dimethylphenyl (1), 4-dimethylphenyl (1), 4-dimethylphenyl (2), 4-dimethylphenyl (3), is readily translated into 4-dimethylphenyl (1), 4-dimethylphenyl (2), 4-dimethylphenyl (3), is readily translated into 4-dimethylphenyl (1), 4-dimethylphenyl (2), 4-dimethylphenyl (3), is readily translated into 4-dimethylphenyl (1), 4-dimethylphenyl (2), 4-dimethylphenyl (3), is readily translated into 4-dimethylphenyl (3), is readily translated into 4-dim

### INTRODUCTION

The development of quantum technologies, such as quantum computing, communication, and sensing, relies on exquisite control over materials design and fabrication.1-3 In these rapidly growing areas of quantum information science (QIS), substantial effort has been devoted to designing, creating, and controlling quantum bits, or qubits, the fundamental units of quantum information processing. 1,4-12 In many impressive proof-ofprinciple QIS demonstrations - such as magnetic resonance of individual proteins,13 entanglement of qubits over a kilometer apart,14 or detection of action potentials of individual neurons<sup>15</sup> - optically active electronic-spin based defects, or color centers, embedded in host crystals, such as the anionic nitrogen vacancy center in diamond, serve as the qubits.1,6,16-21 The ground state spin of these qubits may be optically prepared into an initial state, i.e. initialized, and read out using spin-dependent emission from the color center, enabling remote optical control and single qubit addressability.22,23 While solidstate color centers offer incredible coherence properties and quantum control, deterministic spin localization and defect tunability remain major challenges. Creating designer, optically addressable qubits from the bottom-up represents a modular and scalable approach for emerging quantum technologies.1,8,24-29

Molecular spin-based qubits offer such a pathway for bottom-up design, providing impeccable control over both physical and electronic structure of the qubit.25,28,30-33 Thus, to merge the desirable optical-spin interface of solid-state color centers with the structural modularity of synthetically derived systems, we aim to translate the electronic structure of defects that enables optical-spin initialization and readout into molecular systems. As we have previously outlined, our initial targets for molecular color centers capable of resonant optical-spin initialization and readout require (i) an S = 1 ground state, (ii) an excited state manifold where the first optical transition is an emissive, intra-configurational (i.e. spin-flip) transition that is sufficiently narrow for spin-selective excitation, (iii) a ground state that is addressable with microwaves, and (iv) a ground state spin-lattice relaxation time,  $T_1$ , that is longer than the optical emission lifetime,  $\tau_{opt.}^{34}$  The S=1 ground state is achieved by introducing the proper metal ion into a suitable geometry, such as an octahedral  $d^8$  or tetrahedral  $d^2$  ligand field. The narrow emission linewidths of the intra-configurational transition then arise from the nested potential energy surfaces of the first S = 0 excited state (1ES) and S = 1 ground state (3GS). These two criteria yield the desired electronic structure in Figure 1, where the ¹ES→³GS transition should exhibit narrow emission linewidths for resonant optical initialization and readout. The third criterion enables coherent control of the qubit in order to determine the spin-spin relaxation time,  $T_{\rm m}$ , representing the coherent lifetime of the qubit. The fourth criterion requires that  $T_1$  is sufficiently long or  $\tau_{opt}$  is sufficiently short such that optical excitation and relaxation happens faster than thermal equilibration of the ground spin states, thereby enabling the buildup of ground-state spin polarization.

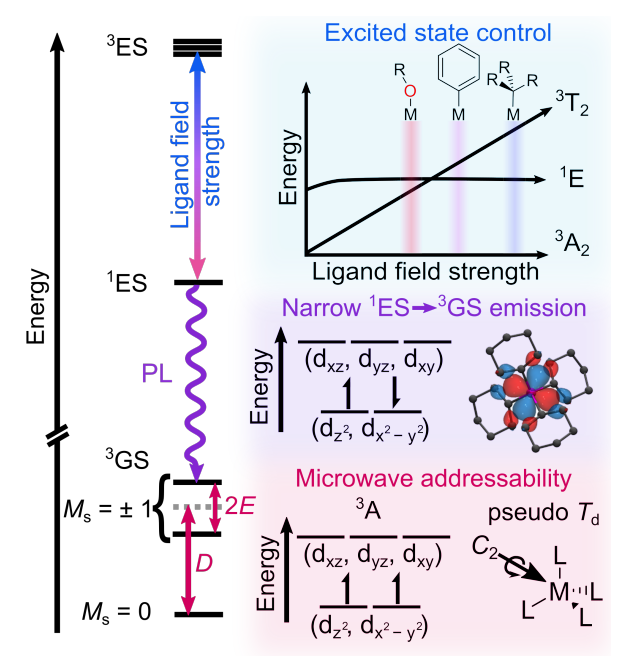


**Figure 1.** General energy level schematic (left) for target electronic structure with molecular symmetry and orbital considerations highlighted (right), including ligand field strength to control the energies of  $^{1}$ ES and  $^{3}$ ES, electron configuration of  $^{1}$ ES and  $^{3}$ ES, and ground state orbital ( $^{3}$ A) and molecular ( $^{7}$ d) symmetry that enable microwave addressability.

With each of these criteria in mind, we previously demonstrated that V3+, Cr4+, and Ni2+ complexes with strong field ligands in trigonal bipyramidal, tetrahedral  $(T_d)$ , or octahedral geometries yield the desired electronic structure for optical addressability.34-37 However, the magnitude of the axial zero field splitting (ZFS) parameter, |D|, for S = 1 transition metal complexes often precludes coherent spin manipulation at the low microwave frequencies (0-40 GHz) that are typically used in optically detected magnetic resonance experiments and conventional electron paramagnetic resonance (EPR) spectrometers. 38,39 To overcome this inherent challenge for these S = 1systems, we initially targeted homoleptic,  $T_d$  CrR<sub>4</sub> complexes, where R is a strong field ligand, which yield small |D| values, which we define as <0.3 cm<sup>-1</sup> or <9 GHz, corresponding to the frequency of an X-band EPR spectrometer. 40-42 In such CrR4 compounds, |D| is minimized by both the orbitally non-degenerate ground state (i.e. 3A) and the high energy excited states that result from the strong ligand field environment (Figure 1).

We recently demonstrated that this bottom-up design approach enabled optical-spin initialization and readout with three S=1,  $Cr(aryl)_4$  compounds, where aryl=2,4-dimethylphenyl, o-tolyl, or 2,3-dimethylphenyl. $^{34}$  Herein, we sought to expand the accessible ligand systems for  $Cr^{4+}$  compounds that enable such optical addressability while modulating the optical-spin interface (Figure 1), a step towards creating bespoke qubits for targeted sensing applications or multi-spin systems for entanglement protocols. While numerous

homoleptic CrR4 compounds have been previously investigated, such as Cr(di-tert-butyl-methylsiloxide)4, Cr(tert-butoxide)<sub>4</sub>, and Cr(dimethylamido)<sub>4</sub>, the inherently poor metal-ligand orbital overlap of the tetrahedral ligand field often proves too weak to achieve the electronic structure in Figure 1.42 To circumvent this issue, we focused on Cr(alkyl)<sub>4</sub> systems, where the strong field alkyl donors result in higher energy spin-triplet excited states than the corresponding aryl compounds (Figure 1) along with suitably small ZFS values for spin manipulation. Additionally, as the energy of the emissive <sup>1</sup>ES is dictated by interelectronic repulsion,<sup>43,44</sup> we chose these  $\sigma$ -only alkyl donors to reduce electron delocalization onto the ligand relative to the Cr-aryl systems. The resulting variation in emission energy demonstrated how the electron delocalization in the Cr4+ species may be used to tune the emission energy through ligand modification or substitution.

Here we describe our investigation of six pseudo- $T_{\rm d}$ , S=1 Cr<sup>4+</sup> compounds: Cr(2,4-dimethylphenyl)<sub>4</sub> (1),<sup>34</sup> Cr(o-tolyl)<sub>4</sub> (2),<sup>45</sup> Cr(2,3-dimethylphenyl)<sub>4</sub> (3),<sup>34</sup> Cr(2,2,2-triphenylethyl)<sub>4</sub> (4),<sup>41</sup> Cr((trimethylsilyl)methyl)<sub>4</sub> (5),<sup>46</sup> and Cr(cyclohexyl)<sub>4</sub> (6)<sup>47</sup> (Figure 2). Comparing Cr(aryl)<sub>4</sub> and Cr(alkyl)<sub>4</sub> compounds, we probed the influence of the ligand field environment on the ground state spin structure and dynamics via continuous-wave (cw) and pulsed EPR spectroscopy. We also used optical absorption and emission spectroscopy along with electronic structure calculations to further characterize the metalligand interactions in these two classes of compounds. These results provide a framework through which to design molecular color centers based on Cr<sup>4+</sup> and illustrate that these principles may be readily extended to other transition metal systems.

#### RESULTS AND DISCUSSION

Synthesis and structural characterization of CrR4 compounds. We synthesized 1-4 according to previously reported methods<sup>34,41,45</sup> via metathesis of CrCl<sub>3</sub>·3(THF) with the corresponding aryl lithium or alkyl lithium salt at -78° C in diethyl ether. 5 and 6 were prepared according to literature procedure<sup>46,47</sup> from the reaction of cyclohexylmagnesium chloride or (trimethylsilyl)methylmagnesium chloride and CrCl<sub>3</sub>·3(THF) at -78° C. When preparing these CrR<sub>4</sub> compounds from either the appropriate organolithium or Grignard reagent, the reaction likely proceeds to the desired Cr4+ product via disproportionation of two CrR3 or [CrR4]- species. For example, two isolable products result from the reaction of (trimethylsilyl)methylmagnesium chloride and CrCl3·3(THF), the tetravalent species, 5, and a cluster of four Cr2+ ions bridged by (trimethylsilyl)methylene ligands, supporting the disproportionation reaction pathway.46 A similar disproportionation reaction pathway is invoked for the formation of Cr(NEt<sub>2</sub>)<sub>4</sub> from Cr(NEt<sub>2</sub>)<sub>3</sub>.48 This reaction pathway provides a theoretical upper limit of 50% based on the metal precursor.

While the molecular structures of **1–3**, **5** and **6** were previously reported,  $^{34,45-47}$  **4** had not yet been structurally characterized and the crystal quality for **5** limited the molecular resolution in previous X-ray diffraction experiments. <sup>46</sup> Thus, we performed single crystal X-ray diffraction experiments for **4** and **5** (Figure 2). The Cr-C bond lengths for all compounds fall in the range of 1.98-2.02 Å, typical for organometallic Cr<sup>4+</sup> compounds, <sup>47,49-51</sup> while the metal site symmetry deviates from ideal  $T_d$  symmetry, as indicated by the space group and the C-Cr-C angles in each structure (Table S6). Although the structural deviation from  $T_d$  is minimal, breaking ideal  $T_d$  symmetry should result in two notable effects for these compounds: (*i*)

introducing non-negligible zero field splitting, *i.e.*, |D| > 0 and (ii) reducing the orbital symmetry of the spin-triplet excited states.<sup>51–53</sup> As a result, the symmetry lowering influences both the ground-state EPR addressability, where large deviations from  $T_{\rm d}$  may result in prohibitively large |D| values, and the optical structure by increasing the number of observable transitions.<sup>52</sup>

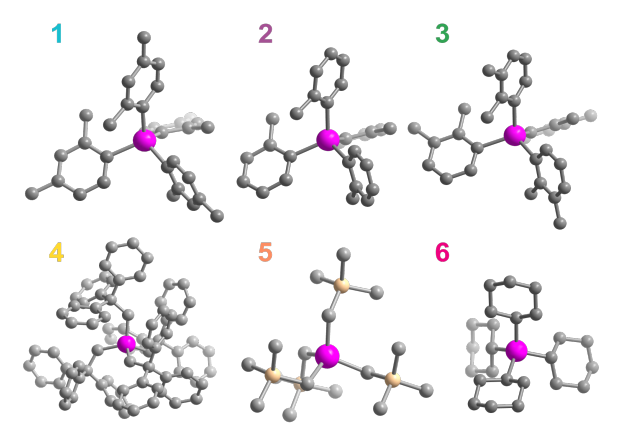


**Figure 2.** Molecular structures of Cr(2,4-dimethylphenyl)<sub>4</sub> (1), Cr(o-tolyl)<sub>4</sub> (2), Cr(2,3-dimethylphenyl)<sub>4</sub> (3), Cr(2,2,2-triphenylethyl)<sub>4</sub> (4), Cr((trimethylsilyl)methyl)<sub>4</sub> (5), and Cr(cyclohexyl)<sub>4</sub> (6). Cr, C and Si given in pink, gray and peach, respectively. Hydrogen atoms omitted for clarity.

Ground state spin structure. To assess the microwave addressability of **4-6**, we turned to X-band cw-EPR spectroscopy. To reduce electronic spin-spin interactions in these measurements, we co-crystallized 5 and 6 in their corresponding, diamagnetic tin analogues, Sn((trimethylsilyl)methyl)4 and Sn(cyclohexyl)4, while we coprecipitated 4 with Sn(2,4-dimethylphenyl)4, 1-Sn (see SI). For all following EPR measurements, we denote the Cr4+ samples diluted in the diamagnetic, Sn hosts as 1'-6'. The cw-EPR spectra in Figure 3 show both a half-field transition around 165 mT ( $g \approx 4$ ), corresponding to the nominally forbidden  $\Delta M_{\rm S}$  = 2 transition, and the full field  $\Delta M_{\rm S}$  = 1 transitions centered around 330 mT ( $g \approx 2$ ). To quantify the ground state spin structure, we simulated the spectra with the spin Hamiltonian  $\hat{H} = D(\hat{S}_z^2 - S(S+1)/3) + E(\hat{S}_x^2 - \hat{S}_y^2) + \sum_i g_i \mu_B \hat{S}_i B_i$ , where D and E are the axial and transverse ZFS parameters, respectively,  $g_i$  is the electron gvalue,  $\mu_B$  is the Bohr magneton,  $\hat{S}_i$  is the spin operator,  $B_i$  is the magnetic field, and i is x, y, or z.

Table 1. cw-EPR spin parameters for 4'-6'.

Sample	<i>D</i>   (GHz)	<i>E</i>   (GHz)	$oldsymbol{g}_{iso}$
4'	2.11	0.5	1.98
5′	1.23	0.11	1.98
<b>6'</b> (site 1) <sup>a</sup>	0.76	0.22	1.9845
<b>6'</b> (site 2) <sup>a</sup>	1.56	0.375	1.9845

 $<sup>^{\</sup>rm a}\,\text{Relative}$  weight fixed at 50% for each site.

While each of these systems likely exhibit anisotropic g-factors, we could not resolve variation in  $g_x$ ,  $g_y$ , and  $g_z$  from these X-band cw-EPR spectra and, thus, simulated each spectrum with an isotropic g-factor.  $\mathbf{4'}$ - $\mathbf{6'}$  exhibit |D| values ranging from 0.76-2.1 GHz with E/|D| ratios of 0.09-0.28 (Table 1). In fact, the cw-EPR spectra of  $\mathbf{4'}$  and  $\mathbf{5'}$  provide ZFS parameters that are consistent with previously reported solution phase values.  $^{40,41}$  Additionally, the rhombicity of  $\mathbf{4-6}$  (i.e. E/|D| > 0) results from a lack of 3-fold or higher rotational axes in the molecular structures.  $\mathbf{2}$  is the only compound investigated here

with a crystallographic structure that enforces |E| = 0 (see below).<sup>34</sup>

The variation in the EPR linewidths and number of turning points (i.e. transitions related to the x, y, or z molecular orientations relative to an external field) in the spectra for the microcrystalline powders of 4'-6' highlight significant differences between each of these samples. For example, the linewidths of the half and full field turning points for 4' are much broader than 1'-3', 5' or 6', suggesting that imperfect lattice matching with the 1-Sn host may lead to significant D- or g-strain of 4.54 Indeed, the line broadening appears similar to  $T_{\rm d}$  Cr<sup>4+</sup> complexes measured in amorphous glassy matrices. 40,55 In contrast, 5' exhibits much sharper linewidths, highlighting the importance of dilution in an isostructural, microcrystalline matrix. Finally, while the spectrum of **6**' shows equally sharp linewidths to 5', the spectrum contains twelve turning points, suggesting that there are two magnetically inequivalent, rhombic S = 1 species in this sample. As a result, this spectrum is appropriately modeled with equally weighted occupation of these two sites with |D| (E) values of 1.56 (0.37) GHz and 0.77 (0.22) GHz (Figure S4). While the exact origin of this effect is unclear, we posit that the unit cell of Sn(cyclohexyl)4 may contain two crystallographically and, consequently, magnetically inequivalent sites that the Cr4+ may occupy (Table S4, see SI for extended discussion). Multiple magnetically inequivalent, S = 1species have been previously observed for frozen solutions of similar samples, such as Cr(1-norbornyl)<sub>4</sub>, Cr(neopentyl)<sub>4</sub>, and Cr((trimethylsilyl)methyl)4, and solid-state samples of Cr(ditert-butylmethylsiloxide)<sub>4</sub>.41,42,55 As a result, all subsequent pulsed EPR data for 6' refer to these two sites as site 1, with |D|

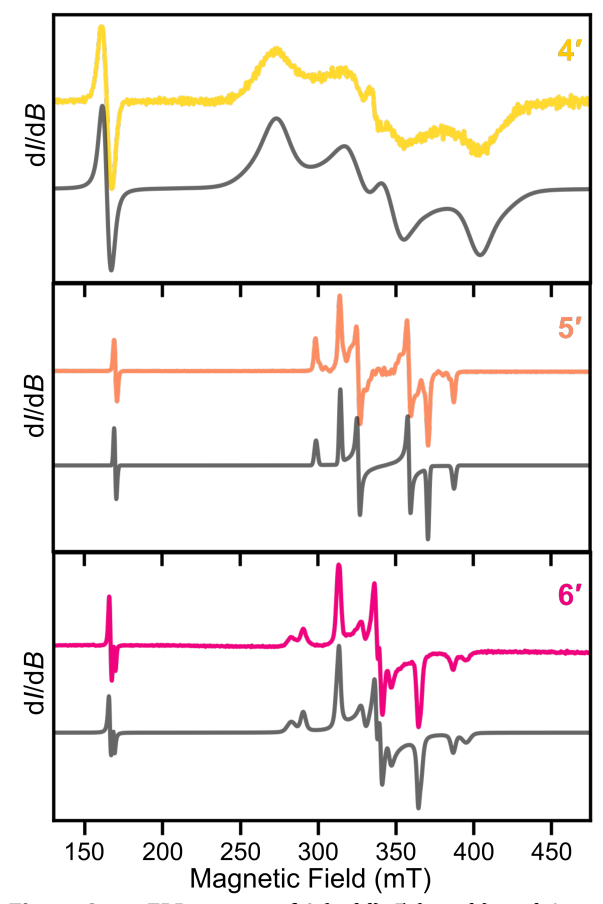


**Figure 3**. cw-EPR spectra of **4** (gold), **5** (peach), and **6** (pink) with simulated spectra in gray (Table 1 and S5).

= 0.76 GHz and E = 0.22 GHz , and site 2, with |D| = 1.56 GHz and E = 0.37 GHz. These results suggest that both lattice matching *and* crystallographic site symmetry may influence the spin properties, such that tuning the host material offers a pathway to readily modulate the ground state ZFS values.

**Ground state spin dynamics.** With 1'-6' displaying suitably small ZFS values for X-band addressability, we investigated the temperature dependence of both  $T_1$  and  $T_m$ . While  $T_m$  represents the coherent information lifetime for the qubit,  $T_1$  represents the time over which spin polarization may accumulate in the ground state for optical spin initialization and imposes an upper limit on  $T_{\rm m}$ . As such, understanding the processes that contribute to both  $T_1$  and  $T_m$  is crucial to evaluate the efficacy of each qubit candidate. We performed echo-detected field swept (EDFS) experiments for 1'-6' to determine the optimal magnetic field for subsequent pulsed experiments (Figure S6). The most intense features correspond to the principal axis of the ZFS tensor oriented perpendicular to the external magnetic field  $(B_0)$ , denoted as transitions along 'xy', while the shoulders at the low and high field extrema arise from the principal axis of the ZFS tensor oriented parallel to  $B_0$ , denoted as transitions along 'z'. For all following temperature-dependent experiments, we present  $T_1$  and  $T_m$  for the higher magnetic field 'y' or 'xy' transitions (except for site 2 of 6'), as these transitions exhibit the greatest absorption intensity in the EDFS spectra (Figures S6, S12-15), allowing us to probe spin relaxation to higher temperatures than the weaker, 'z' transitions. We discuss the orientation dependence of  $T_{\rm m}$  in greater detail below.

We measured  $T_1$  using an inversion recovery sequence,  $P_1$ -T- $\pi$ /2- $\tau$ - $\pi$ - $\tau$ . The resulting data were fit with the stretched exponential function, I = -A {exp[ $-(\tau/T_1)^B$ ]  $-I_0 - 1$ }, where the stretch factor, B, is required to best model the inversion recovery curves below 20 K. Typical B values for these compounds below 15 K are 0.5-0.75. At low temperatures,  $\mathbf{2}'$ ,  $\mathbf{3}'$ ,  $\mathbf{5}'$  and  $\mathbf{6}'$  (site 2) exhibit the longest  $T_1$  times on the order of 1-5 ms, while  $\mathbf{1}'$ ,  $\mathbf{4}'$  and  $\mathbf{6}'$  (site 1) exhibit the shortest  $T_1$  times of 0.1-0.4 ms (Figure 4). As temperature increases to 40 K,  $T_1$  decreases sharply to 1-3  $\mu$ s for all compounds. Notably, these  $T_1$  times for all compounds are substantially longer than the  $\tau_{\rm opt}$  lifetimes determined for  $\mathbf{1}'$ - $\mathbf{3}'$ ,  $\mathbf{3}^4$  suggesting that these compounds meet the fourth criterion outlined above.

To understand this relaxation behavior, we considered three possible processes that may contribute to  $T_1$  in this temperature range: the direct process, a Raman process, and an Orbach-Aminov process.<sup>56,57</sup> To model these processes, we used the following equation,

$$\frac{1}{T_1} = A_{\text{Dir}} T + A_{\text{Ram}} \left(\frac{T}{\theta_{\text{D}}}\right)^9 J_8 \left(\frac{T}{\theta_{\text{D}}}\right) + \frac{A_{\text{Orb}}}{\left(e^{\frac{\theta_{\text{Orb}}}{T}} - 1\right)}$$

where  $A_{\rm Dir}$ ,  $A_{\rm Ram}$  and  $A_{\rm orb}$  are the coefficients for the direct, Raman and Orbach-Aminov relaxation processes, respectively, T is the temperature,  $\theta_{\rm D}$  is the Debye temperature,  $J_{\rm B}$  is the transport integral and  $\theta_{\rm Orb}$  is the Orbach temperature corresponding to the energy of the excited state involved in the relaxation process. With the limited temperature range for these systems, these data were most accurately modeled with Orbach-Aminov and Raman processes while the direct process often had a near negligible contribution to  $T_{\rm I}$ , even below 10 K (Tables S21-S22).

Inclusion of an Orbach-Aminov process in the fitting procedure and stretch factors close to 0.5 at low temperature suggest that electronic spin interactions and/or spectral diffusion may contribute to low temperature  $T_1$  relaxation.<sup>29,57</sup> Such behavior could arise from spin aggregation providing a cross relaxation pathway.<sup>57-61</sup> Thus, we calculated the approximate molarity of Cr4+ ions of each sample based on approximate densities from the single crystal structures and relative ratio of Cr4+: Sn4+ determined from inductively coupled plasma optical emission spectrometry (Table S8). The concentrations ranged from 7-40 mM where samples displaying the shortest  $T_1$  values typically have the highest relative Cr4+ concentrations, suggesting that electronic spin interactions contribute to  $T_1$  at low temperatures. To further validate this observation, we performed a similar fitting procedure as previously outlined<sup>57</sup> and found that the  $\Theta_{\rm Orb}$  values for 1'-6' (Table S21, Figure S9) fall in the expected range for interactions with dipolar coupled electronic spin dyads or triads (see SI for details).57,59-61

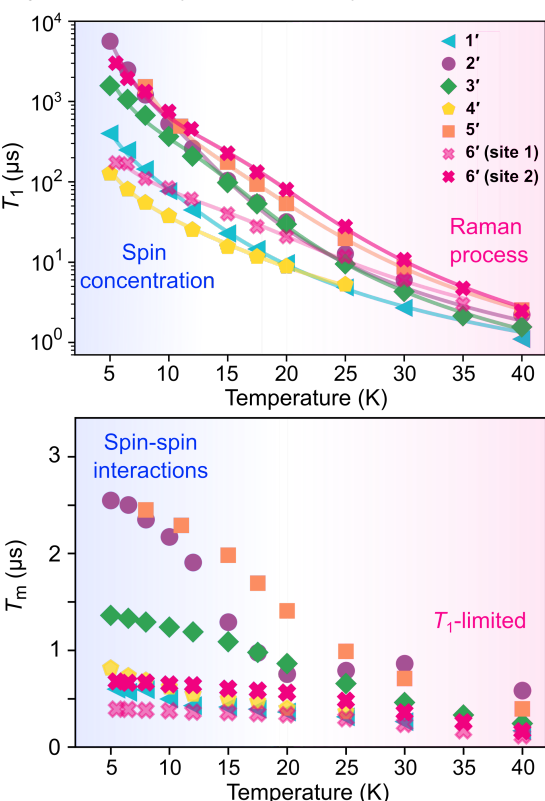


**Figure 4.** Temperature dependence of  $T_1$  (top) and  $T_m$  (bottom) for  $\mathbf{1'}$ – $\mathbf{6'}$ . Solid lines represent best fits of temperature dependent relaxation processes discussed in the main text. Blue and pink regions highlight the impact of electronic spin concentration (spin-spin interactions) and Raman mediated ( $T_1$ ) processes, respectively, on  $T_1$  ( $T_m$ ).

To further probe the effect of electronic spin concentration on  $T_1$ , we performed  $T_1$  measurements on  $\mathbf{2'}$  while varying the ratio of Cr<sup>4+</sup>:Sn<sup>4+</sup>. Between 5 and 10 K, the  $T_1$  times are longer for lower spin concentrations, (Figure S7 inset) while the high temperature  $T_1$  times are nearly identical across all samples. These data further suggest that a concentration-dependent cross-relaxation process dictates lower temperature relaxation while the higher temperature  $T_1$  relaxation is dominated by a concentration-independent Raman process. <sup>59</sup> Most notably, the similarity in the higher temperature  $T_1$  times of all samples in Figure 4 illustrates the need to understand the

phonon modes that mediate relaxation in these systems. Thus, accessing optically addressable molecular systems with higher operation temperatures will require further molecular design, such as increasing ligand denticity, ligand rigidity, or metal-ligand covalency, and analysis of operative phonon modes mediating relaxation.<sup>30,62-64</sup>

We then measured the spin coherence,  $T_{\rm m}$ , using the Hahnecho sequence,  $\pi/2$ - $\tau$ - $\pi$ - $\tau$ . The resulting decay curves were fit with the monoexponential decay function,  $I = I_0 \left[ \exp(-2\tau/T_{\rm m}) \right]$ . Below 10 K, we found that  $\mathbf{2'}$ ,  $\mathbf{3'}$  and  $\mathbf{5'}$  exhibited the longest  $T_{\rm m}$  times between 1.36–2.55  $\mu$ s while  $\mathbf{1'}$ ,  $\mathbf{4'}$  and  $\mathbf{6'}$  (sites 1 and 2) displayed shorter  $T_{\rm m}$  times from 0.39–0.82  $\mu$ s (Figure 4). By then measuring  $\mathbf{2'}$  in toluene-d<sub>8</sub>,  $T_{\rm m}$  increased to 5.7  $\mu$ s at 3.6 K, suggesting that the high density of environmental  $^1$ H nuclear spins in these solid state samples may limit  $T_{\rm m}$  at low temperatures.

While  ${}^{1}H$  nuclear spins likely limit the upper bound of  $T_{\rm m}$ for all of these systems, high concentration of Cr4+ and/or aggregation of Cr4+ during co-crystallization may further reduce  $T_{\rm m}$ . Indeed, the Cr<sup>4+</sup> molarities ranged from ~7 mM to ~40 mM (Table S8), which is relatively high compared to pulsed EPR experiments in solution or frozen glassy matrices.30-32,65,66 Generally, the samples with lowest concentrations, such as 2' and 3', exhibit longer  $T_{\rm m}$  times, while more concentrated samples, such as  $\mathbf{1}'$ , exhibit  $T_{\rm m}$  times nearly three times shorter despite similar <sup>1</sup>H environments between 1', 2', and 3'. Indeed, increasing the Cr4+ concentration for 2' from 7 to 22 mM results in a four-fold reduction of T<sub>m</sub> (Figure S7). These initial investigations illustrate that higher spin dilution or alternative crystallization conditions may mitigate electronic spin- spin interactions, offering an immediate pathway to improve  $T_{\rm m}$  for each of these compounds. For example, the longer than expected  $T_{\rm m}$ for 5', a sample with high Cr4+ concentration, could result from improved distribution of Cr4+ sites during co-crystallization.

With increasing temperature,  $T_{\rm m}$  for  ${\bf 1'}$  and  ${\bf 3'}$ - ${\bf 6'}$  are approximately temperature independent until around 15 K, at which point  $T_{\rm m}$  begins to decrease. In contrast,  $T_{\rm m}$  for  ${\bf 2'}$  exhibits a sharp decrease until 20 K, followed by a slight recovery until 30 K at which point,  $T_{\rm m}$  declines again (see SI for further discussion). These data illustrate that  $T_{\rm m}$  is limited by  $T_{\rm 1}$  at temperatures >35 K for *every* compound. This upper bound that  $T_{\rm 1}$  imposes on  $T_{\rm m}$  renders coherent spin manipulation challenging above 60 K. For many sensing applications, pushing this temperature limit up to 77 K and beyond will be critical, further highlighting the need to design S=1 transition metal compounds that exhibit measurable  $T_{\rm 1}$  at higher temperatures.

**Orientation dependence of**  $T_{m}$ **.** Previous studies with  $S = \frac{1}{2}$ transition metal-based systems have demonstrated that coherence times vary as a function of molecular orientation with respect to an external magnetic field (denoted as  $B_0$ ), for example, due to librational motion.65,66 Alternatively, hyperfine-mediated relaxation mechanisms have dictated the orientation-dependent T<sub>2</sub> times for NV<sup>-</sup> centers.<sup>67</sup> Further understanding this orientation dependence is critical when designing molecular vector-based magnetic field sensors analogous to solid-state color centers.<sup>68-71</sup> From the EDFS spectra of the microcrystalline powder samples of 1'-6', we observe all possible orientations of our molecular systems that are separated over a readily accessible field range (200-500 mT) by the non-zero ground-state ZFS (Figure S6). This spread of transitions allows us to probe  $T_{\rm m}$  as a function of molecular orientation relative to Thus, we performed field-dependent Hahn echo

experiments across the magnetic field range of these EDFS spectra. The spin bath of  $^1\mathrm{H}$  spins resulted in significant electron spin echo envelope modulation (ESEEM) at fields below ~330 mT (Tables S23-28). Thus, the fitting procedure for the resulting decay curves accounted for this ESEEM with the function:  $I = I_0$  {1 –  $B\cos(\omega \tau + d)$  [exp(-2 $\tau/T_{\rm osc}$ )]} [exp(-2 $\tau/T_{\rm m}$ )]+ f, where B is the ESEEM amplitude,  $\omega$  is the (angular) ESEEM frequency in MHz, d is the modulation phase,  $T_{\rm osc}$  is the ESEEM decay time, and f is an offset term.

In Figure 5a, we overlaid the magnetic field dependence of  $T_{\rm m}$  with the corresponding EDFS spectrum for  ${\bf 2'}$ . This EDFS spectrum is a summation of the transitions between  $M_{\rm S}=0$  and  $M_{\rm S}=-1$  (green) and between  $M_{\rm S}=0$  and  $M_{\rm S}=+1$  (pink) as depicted in Figure 5b. The shoulders at 220 and 485 mT arise from molecules with the principal axis of the ZFS tensor oriented parallel to  $B_0$ , denoted as transitions along 'z'. The two more intense peaks at 275 and 410 mT correspond to 'xy' transitions where the principal axis of the ZFS tensor is oriented perpendicular to  $B_0$ . From single crystal optically detected

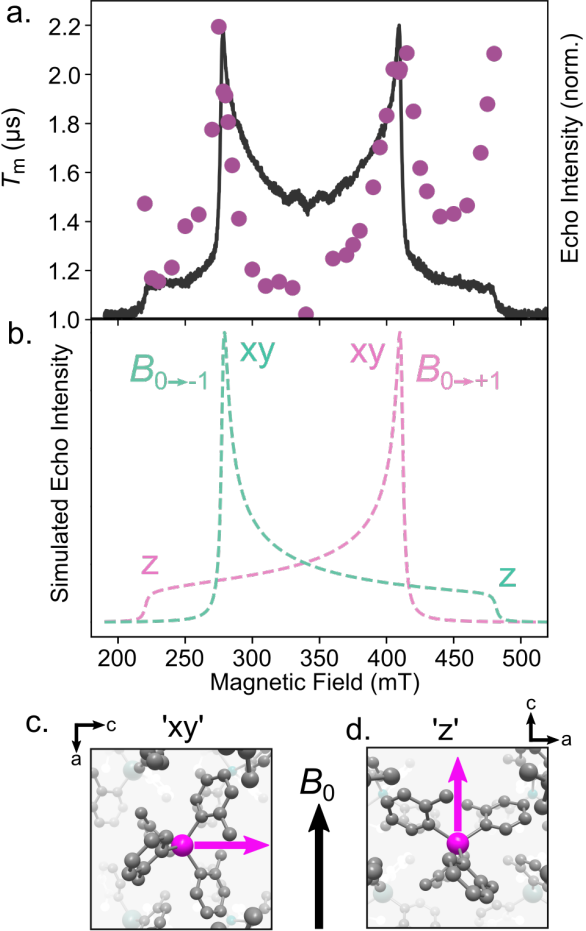


**Figure 5.** (a) X-band magnetic field dependence of  $T_{\rm m}$  (purple circles) for  ${\bf 2'}$  at 10 K overlaid on the corresponding echo-detected field swept spectrum (black). (b) Decomposition of transitions between  $M_{\rm S}=0$  to  $M_{\rm S}=-1$  ( $B_{0\rightarrow-1}$ , green) and  $M_{\rm S}=0$  to  $M_{\rm S}=+1$  ( $B_{0\rightarrow+1}$ , pink), the sum of which result in the EDFS spectrum in (a). (c, d) Crystallographic orientation of  ${\bf 2'}$  highlighting the principal axis of the ZFS tensor (pink arrow), aligned perpendicular (c) and parallel (d) to the external magnetic field,  $B_0$  (black and gray arrows). The crystallographic a and c axes are given for each orientation. See Figure S11 for filled unit cell.

magnetic resonance experiments, we found that *D* is oriented along the crystallographic *c* axis, colinear with the *S*<sup>4</sup> improper rotation axis of the central molecule (Figures 5 and S11).34 For 2', the molecules with the principal axis of the ZFS tensor oriented parallel or perpendicular to  $B_0$  (e.g. 220, 275, 410, and 485 mT), as shown in Figure 5c, exhibit  $T_{\rm m}$  times roughly 2 times longer than molecules at intermediate orientations. This orientation dependence of  $T_{\rm m}$  is similar to  $S = \frac{1}{2}$  systems, where the longest  $T_{\rm m}$  times occur for molecules with the principal axes of the g matrix or hyperfine tensor oriented parallel or perpendicular to  $B_0$ .65,66 These data clearly illustrate that orienting the highest order rotational axis of  $S > \frac{1}{2}$  molecular spins parallel or perpendicular to an applied external field can help maximize coherence times in the high field limit (i.e.  $g_i\mu_B B_0 > |D|$ ), assuming that the rotational axis contains the principal axis of the ZFS tensor.<sup>73</sup> However, precisely assigning the dominant orientation-dependent relaxation mechanisms in S = 1 molecular systems will require higher field and frequency pulsed EPR studies to deconvolute the influence of librational and hyperfine-mediated decoherence pathways.65,66,74

For the compounds with  $E \neq 0$ , we observe six total local maxima since  $x \neq y$  in the EDFS spectra<sup>75</sup> (see Figure S12-S15, Tables S23-S28). We find a similar relationship between molecular orientation and  $T_m$ . For  $\mathbf{1}'$  and  $\mathbf{5}'$ ,  $T_m$  appears to increase

at the canonical x, y and z orientations, while  ${\bf 3'}$  and  ${\bf 6'}$  show the longest  $T_{\rm m}$  values when the principal axis of the ZFS tensor is parallel to  $B_0$  (i.e. along 'z'). These collective data illustrate that field-dependent analysis is crucial to accurately compare the  $T_{\rm m}$  times of molecular systems, which may show large variations in  $T_{\rm m}$  as a function of orientation.

Excited state structure. To evaluate the excited state structure of these CrR4 systems, we coupled steady state absorption and emission spectroscopy with electronic structure calculations. The UV-Vis-NIR absorption spectra in Figure 6 illustrate that all compounds exhibit more than two excited state transitions in these solution spectra, in line with the symmetry lowering from  $T_d$  observed in the molecular structures. Similar behavior was noted for related homoleptic, T<sub>d</sub> Cr<sup>4+</sup> and isoelectronic V3+ complexes, where the solution symmetry was described as  $C_{2v}$  or  $D_{2d}$ . 35,51,52 For **1-3**, we observe five distinct features in the visible and NIR regions with similar molar absorptivities ( $\epsilon \sim 1000-1200~M^{-1}~cm^{-1}$ ) from 500-800 nm (Figure S17). These three spectra are nearly identical as a result of the similar donor strength of the three different aryl ligands. When substituting the aryl donors with stronger, σ-donating alkyl ligands in 4-6, the absorption spectra show a corresponding increase in the spin-triplet excited state energies with a less intense transition from 580-700 nm and a more intense

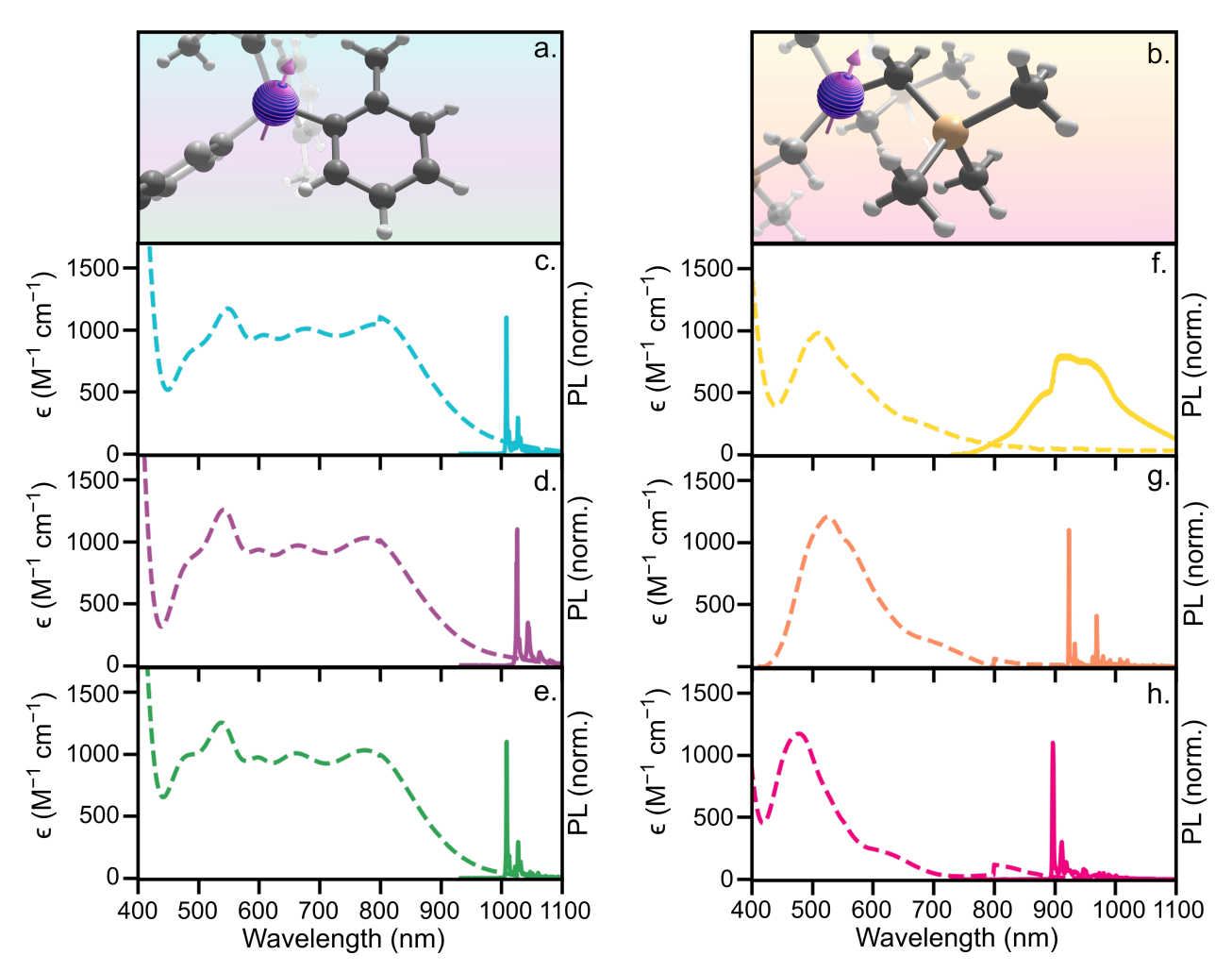


**Figure 6.** (a,b) Molecular structures of **2** (a) and **5** (b) highlighting the variation in metal-ligand bonding between Cr-aryl and Cr-alkyl systems with Cr, C, Si and H given as purple, gray, peach and white, respectively. (c-h) Room temperature UV-Vis-NIR spectra in toluene (dashed lines) and 4 K PL spectra in diluted solid-state matrix (solid lines) of **1** (c), **2** (d), **3** (e), **4** (f), **5** (g), and **6** (h).

asymmetric absorption band between 420 and 650 nm. This trend in donor strength is corroborated by both the calculated absorption spectra (Figure 7 and Figure S18) and the increasingly negative Cr<sup>4+/3+</sup> redox potential for **4-6** relative to **1-3** (Figure S16).

We performed electronic structure calculations of 1-6 to further elucidate the differences between these homoleptic aryl and alkyl compounds. The geometries of 1-6 were optimized in their spin-triplet ground states using unrestricted Kohn-Sham<sup>76,77</sup> density functional theory (B3LYP+D3BJ/def2-TZVP)<sup>78-85</sup> as implemented in ORCA.<sup>86</sup> Excited states were then calculated and analyzed using time-dependent DFT (TDDFT),87-89 which provides a reasonable description of excitations in transition-metal complexes.90,91 The calculated spectra of 2 and 6 shown in Figure 7 are representative of the spectra for the other aryl and alkyl compounds, respectively (Figure S18). The individual transitions are depicted as sticks with hollow circles whose height is proportional to the oscillator strength. The calculations predict that 2 has a broad range of spectral intensity, with both lower and higher energy transitions exhibiting moderate to high intensities. In contrast, the three lowest energy transitions for 6 exhibit very weak intensity while the three higher energy transitions exhibit stronger intensity. These predictions are in good agreement with the experimentally measured spectra shown in Figure 6, indicating that this level of theory provides an accurate description of the electronic structure of these complexes. Similar qualitative agreement is observed for the spectra of the other complexes 1 and 3-5 (Figure S18). Absorption spectra for 1-6 obtained using the complete active space self-consistent field method89 (not shown) were found to be similar to the TDDFT results.

To understand the differences in the spectra between the Cr(aryl)<sub>4</sub> and Cr(alkyl)<sub>4</sub> compounds, we characterized the TDDFT transitions of **1-6** using natural transition orbitals (NTOs).<sup>92</sup> NTOs are combinations of molecular orbitals for each

excited-state transition resulting in unique "electron" and "hole" orbital pairs ranked by their contributions. Analysis of the NTOs shows that the "electron" orbital of all transitions in both **2** and **6** is essentially the same and corresponds to a hybridization of Cr  $d_{xy}$  and  $p_z$  orbitals. For all compounds, the NTOs indicate that the first six spin-allowed transitions are largely metal centered (Figures 7 and S19-S24), as expected from transition metal systems of  $C_{2v}$  or lower symmetry. <sup>49,50</sup> These six transitions naturally separate into three transitions with weak intensity and three transitions with strong intensity. All weak-intensity transitions have a  $d_x^2$ - $y^2$  "hole" orbital, and all strong-intensity transitions have a  $d_z^2$  "hole" orbital. These results agree with symmetry selection rules for  $T_d$  symmetric  $d^2$  ions, where transitions to  ${}^3T_2$  are symmetry-forbidden and to  ${}^3T_1$  symmetry-allowed (see SI for further discussion). <sup>53</sup>

While the transitions in 2 are qualitatively identical to those of 6, their relative ordering is unique. Specifically, the second transition of **2** has the same  $d_{z^2}$  "hole" orbital as that of the fourth, fifth, and sixth transitions of 6, resulting in strong transition intensity. This identical orbital character is directly visualized with the NTOs of the second transition of 2 and the fourth transition of 6 (Figure 7). The NTOs also exhibit increased delocalization in 2, likely due to the potential for both  $\pi$ - and  $\sigma$ -bonding interactions with the aryl ligands, whereas the alkyl ligands only allow for  $\sigma$ -bonding. This difference in ligand interactions is likely responsible for the greater degree of symmetry breaking in 1-3, which reorders the excited-state manifold as compared to an ideal  $T_d$  symmetric  $d^2$  metal and results in the wider absorption spectra relative to 4-6. While these spin-allowed transitions are not used for resonant initialization and readout schemes, we expect similar orbital symmetry properties to influence the  ${}^{1}ES \rightarrow {}^{3}GS$  emissive transition. Moreover, controlling the metal-ligand orbital interactions involved in the spin-triplet excited states, and hence their transition intensity, may enable off-resonant optical initialization and readout pathways, similar to defect-based spin centers.1,17

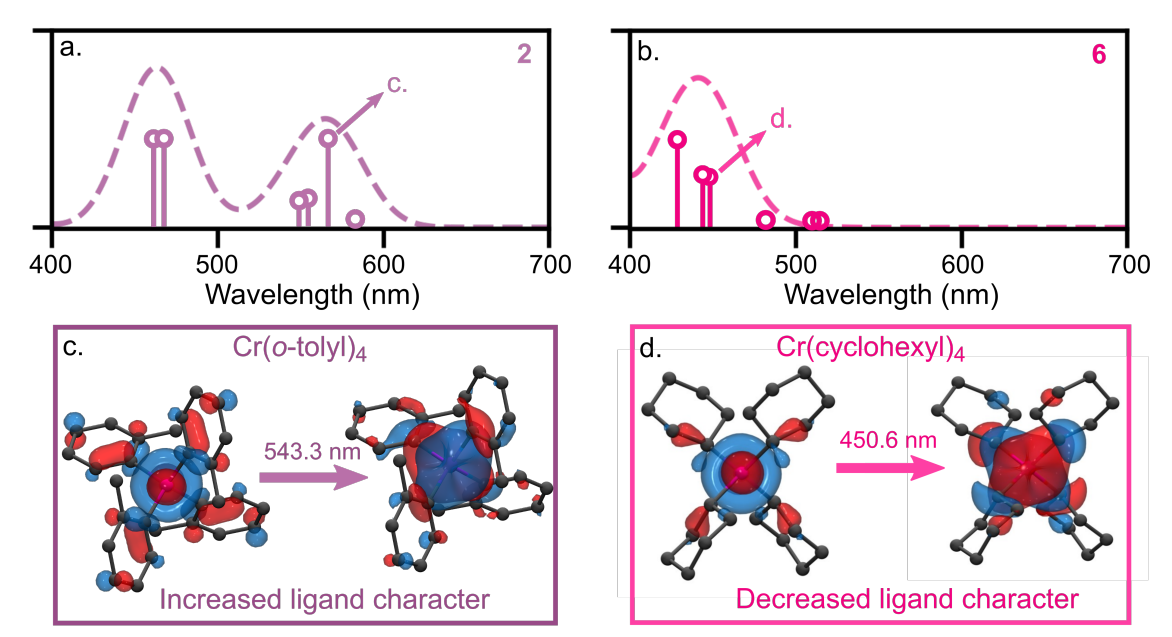


**Figure 7.** (a, b) Normalized TDDFT absorption spectra of **2** (a) and **6** (b) with a Gaussian broadening width of  $\sigma$  = 20 nm. Excitations with relative oscillator strengths are given as sticks. (c, d) NTOs with contributions >96% for the second and fourth spin-triplet excitations of **2** (c) and **6** (d) indicated by arrows on the calculated absorbance spectra. For each excitation, the "hole" and "electron" orbitals are given on the left and right of the arrow, respectively.

We then experimentally evaluated the impact of varying alkyl donors on the emission energies with photoluminescence (PL) spectroscopy. Previously, we found that 1'-3' exhibit narrow emission between 1010-1025 nm from a spin-singlet excited state.<sup>34</sup> To test if we observe similar behavior for **4'-6'**, we diluted these compounds in the same host used for the EPR measurements. For all compounds except 4', emission from this spin-singlet state shows a narrow zero-phonon line (ZPL) with a well-resolved vibrational side band. 1'-3' exhibit ZPLs from 1010-1025 nm (9,756-9,911 cm<sup>-1</sup>) and **5'** and **6'** exhibit ZPLs from 897-923 nm (10,834-11,148 cm<sup>-1</sup>). The  $\sigma$ -only alkyl donors result in higher energy spin-singlet excited states, as was observed for their spin-triplet excited states. The higher energy emission in 4'-6', relative to 1'-3', may be explained by the increased exchange energy in more localized orbitals of the Cr-alkyl compounds.

Such narrow ZPLs for 1'-3', 5' and 6' are indicative of a transition between two states with nested potential energy surfaces, as expected for an intra-configurational, spin-flip transition from the spin-singlet excited state to spin-triplet ground state (Figure 1).<sup>36,93-95</sup> In fact, optimizing the spin-singlet geometries of 1-6 with DFT yields metal-centered valence orbitals that are similar to those of the triplet ground state, as expected for these intra-configurational transitions. Using DFT, we calculated the singlet-triplet gaps at the singlet-optimized geometry, as an estimate of the ZPL. The results (Table S31) provide good quantitative agreement with the experimental values for 1-3, but less accurate results for 4-6 (see SI for further discussion).

**Cumulative energy level diagram.** Summarizing the results from the EPR and optical experiments as well as TDDFT calculations, we constructed simplified energy level diagrams for **1-6** (Figure 8). These energy diagrams illustrate that each compound exhibits the targeted electronic structure where the first excited state is a spin singlet that exhibits radiative decay to the ground state (Figure 1). These results also highlight that a strong ligand field, high symmetry environment is crucial to achieve *both* the desired excited state structure and microwave addressability. For example, the improved metal-ligand orbital

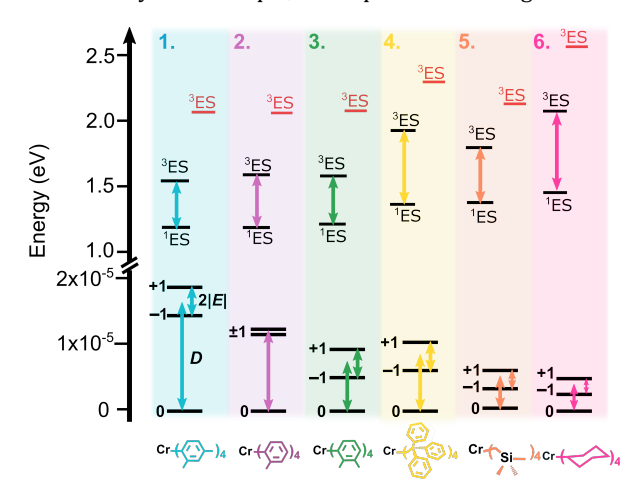


**Figure 8.** Overall energy level diagram for **1-6**. ZFS values were determined from cw-EPR experiments at 77 K and the experimental excited states (black) were approximated from PL experiments at 4 K and from the deconvolution of the UV-Vis-NIR absorption spectra in Figure S17. The first TDDFT spin-triplet excitation energies are given in red.

overlap in trigonal bipyramidal geometries, relative to tetrahedral, around Cr4+ likely yield the targeted electronic structure, but the non-cubic symmetry may result in ZFS values that preclude X or Q-band EPR addressability.  $^{35,36}$  Alternatively, pseudo- $T_{\rm d}$  tetrasiloxide or tetraalkoxide Cr4+ complexes yield relatively small ZFS values for microwave addressability, but the ligand fields are likely too weak to boost the energy of the spin-triplet excited states above the energy of the spin-singlet excited state.  $^{42,96}$  Thus, the appropriate design of these Cr4+ compounds, or related spin qubits, necessitates simultaneous consideration of ground state spin properties and excited state structure to achieve the desired optical-spin interface.

Designing the next generation of optically addressable Cr4+ **compounds.** Ground state spin considerations: **1-6**, along with the rich literature on tetrahedral Cr<sup>4+</sup> compounds, offer valuable insight for the creation of future optically addressable molecular systems. 40-42,97 These compounds demonstrate a trend for controlling the ground-state spin structure. Specifically, 4-6 and related Cr(alkyl)4 compounds show generally smaller ZFS values than Cr(aryl)<sub>4</sub> compounds, such as 1-3, Cr(2,6-dichlorobenzene)4 or Cr(pentachlorophenyl)4.34,40,41,51,55,98 More broadly considering homoleptic CrR4 compounds, these variations in ZFS between Cr(alkyl)<sub>4</sub> and Cr(aryl)<sub>4</sub> agree generally with the principle that |D| trends inversely with ligand field strength. For example, in general, |D| for  $Cr(alkyl)_4 < Cr(alkox$ ide)<sub>4</sub> < Cr(siloxide)<sub>4</sub> because the stronger ligand field raises the energy of the spin-triplet excited states, reducing spin-orbit mediated coupling between the spin-triplet ground state to these excited states and effectively minimizing |D|.<sup>42,53,96</sup> Thus, the choice of ligand environment directly modulates the ground state spin structure, where stronger field ligands should give rise to generally smaller |D| values. However, the coherent spin manipulation of these compounds is currently limited at higher temperatures by the  $T_1$  times in every case. Thus, beyond ligand field strength considerations, predicting vibrational contributions to relaxation and selectively eliminating those pathways to mitigate such relaxation represents a crucial next step.99,100 In parallel, Tm should be readily improved with ligand deuteration, as shown from toluene-d<sub>8</sub> measurements, and/or dynamical decoupling routines, offering immediate pathways for both further chemical and physical means to lengthen  $T_{\rm m}$ .

Excited state considerations: Appropriate ligand design may tune the emission energy into desirable regions such the NIR for biological sensing101 or the telecommunications band for quantum optical networking.20 For example, increased substitution on the  $\alpha$  carbon in **6** results in the highest energy ZPL. The greater  $\alpha$  carbon substitution of the cyclohexyl ligand increases its nucleophilicity, or basicity, relative to (trimethylsilyl)methyl or 2,2,2-triphenylethyl, preventing substantial spin delocalization from the metal onto surrounding ligands. Such increased spin localization on the metal increases the interelectronic repulsion of the spin-paired <sup>1</sup>ES, resulting in a higher energy ZPL for 6' relative to 5'.44,102 Additionally, the absorption spectra of 5 and its neopentyl analogue, Cr(CH2C(CH3)3)4, indicate that substituting the trimethylsilyl  $\beta$  carbon substituent in **5** for the more electron donating *t*-butyl substituent increases the  $\sigma$ -donation strength, <sup>41</sup> offering another handle to modulate spin delocalization in the <sup>1</sup>ES. As a result, appropriate choice of  $\alpha$  and  $\beta$  carbon functionalization may finely tune the singlet state energy in Cr(alkyl)<sub>4</sub> compounds.

Similarly, the higher energy emission in 4'-6', relative to 1'-3', can be explained by the increased exchange energy in the

localized metal-centered orbitals involved in the  ${}^1\text{ES} \rightarrow {}^3\text{GS}$  transition for  $4'\text{-}6.^{43,44,53}$  To further modulate this optical readout handle in Cr(aryl) ${}^4$  systems, introducing electron withdrawing groups onto the aromatic ring should reduce the aryl electron donation into the metal center and result in lower energy emission. Thus, controlling the metal-ligand interactions provides a powerful design parameter to tune emission into desirable wavelength regions for optical spin-based sensing applications. Crucially, accurate theoretical predictions of the challenging multiconfigurational singlet-state energies may enable more rapid iterative design of molecular qubits emitting at targeted wavelengths.

Beyond emission energies, our results also illustrate that only  $\bf 5'$  and  $\bf 6'$  exhibit appropriately narrow optical linewidths for the resonant optical initialization and readout used for  $\bf 1'$ - $\bf 3'$ , while the emission from  $\bf 4'$  is likely too broad for such schemes. To avoid broadening optical linewidths, introducing ligands with increasing denticity or greater structural rigidity may reduce ligand fluxionality, especially in non-crystalline hosts, as shown with a tren-based  $V^{3+}$  system.  $^{36}$  In particular, maintaining the desired linewidths in amorphous matrices may be important for biological sensing applications. Given that decreasing ligand fluxionality may both elongate  $T_1$  at higher temperatures and reduce optical linewidth broadening,  $C_3$ -symmetric strong-field ligand scaffolds with  $d^2$  metal ions may offer valuable molecular targets.

Chemical stability considerations: The air stability of 4 suggests that peripheral ligand functionalization offers routes to target both air stability and biological compatibility. For example, appropriately functionalized, sterically hindered ligands, such as norbornyl or adamantyl derivatives, where  $\alpha$  hydride elimination is impossible and  $\beta$  hydride elimination is incredibly unfavorable,  $^{97}$  may give rise to even more stable Cr(alkyl)4 complexes. In fact, 5 and Cr(1-norbornyl)4 have been shown to persist in the presence of dilute acids,  $^{46,103}$  suggesting derivatized Cr(alkyl)4 derivatives may be stable in the presence of water or other biologically relevant conditions. However, these compounds would clearly require appropriate ligand functionalization to generate water compatible systems, a goal that may instead be achieved through generation of solution-based self-assembled nano structures.

#### **CONCLUSIONS**

The combination of cw-EPR, pulsed-EPR and optical spectroscopies coupled with theoretical investigation demonstrates that 4-6 exhibit the desired electronic structure for optically addressable molecular qubits. 5 and 6 exhibit suitably narrow photoluminescence linewidths for resonant optical initialization and readout, similar to 1-3. These compounds illustrate that chemical control over the Cr4+ environment may be leveraged to design and optimize specific features of optically addressable molecular qubits. Crucially, these six systems demonstrate the impact of ligand identity on the energy of the spin-singlet excited state that is used in resonant optical initialization and readout schemes. The combination of these features provides opportunities for bottom-up qubit design to meet challenges in disparate QIS fields, including tuning the emission energy into the telecommunications band for quantum optical networking, synthesizing water soluble and air stable compounds for biological sensing and targeting qubit-substrate interactions for sensing of emergent materials. To meet this broad range of challenges, further exploration of CrR4 compounds and extension of the desired electronic structure into

heteroleptic compounds as well as related S = 1, {MR<sub>4</sub>} systems represent key next steps.

#### ASSOCIATED CONTENT

The Supporting Information is available free of charge at [DOI]including full crystallographic data for **4**, **5** and **10** and additional EPR, optical, electrochemistry and computational data and discussion.

### **AUTHOR INFORMATION**

## Corresponding Authors

### **Author Contributions**

All authors have given approval to the final version of the manuscript.

## **Funding Sources**

We acknowledge support from the US Army Research Office under award number W911NF2010088 for the synthesis (D.W.L and D.E.F.) and calculation (A.K. and T.C.B.) of new molecular color centers. S.L.B., L.R.W., and D.D.A acknowledge funding from ONR N00014-17-1-3026 and Tohoku University for execution of optical measurements. D.E.F. and D.D.A. acknowledge support for the integration of molecules into a larger quantum infrastructure from the U.S. Department of Energy Office of Science National Quantum Information Science Research Centers. T.G. acknowledges support from the NSF under award number CHE-1848369. S.M.G. acknowledges support from the Molecular Sciences Software Institute, which is funded by NSF under award number OAC-1547580. K.A.C. acknowledges support from the NSF GRFP through DGE-11842165. This work made use of the IMSERC Crystallography facility at Northwestern University, which has received support from the Soft and Hybrid Nanotechnology Experimental (SHyNE) Resource (NSF ECCS-2025633), and Northwestern University. Major funding for the Bruker EMXPlus was provided by National Science Foundation Award 1726244 (2017) to the School of Chemical Sciences EPR lab at the University of Illinois. This work also made use of the Caltech EPR facility, which is supported by the NSF (NSF-1531940) and the Dow Next Generation Educator Fund. Metal analysis was performed at the Northwestern University Quantitative Bio-element Imaging Center. The Flatiron Institute is a division of the Simons Foundation.

#### Notes

The authors declare the following competing financial interests: D.W.L., S.L.B., P.J.M., D.E.F., and D.D.A. are inventors on patent application no. 63008589 submitted by the University of Chicago that covers chemically tunable optically addressable molecular-spin qubits and associated methods. P.J.M. is a paid consultant to ARCH Venture Partners.

## **ACKNOWLEDGMENT**

EPR data were collected at the School of Chemical Sciences EPR lab at UIUC and at the Caltech EPR facility. The authors kindly thank Dr. Toby Woods, Dr. Paul Oyala and Rebecca Sponenburg for experimental assistance with EPR and ICP-OES measurements. The authors thank Dr. Michael Wojnar and Mykyta Onizhuk for helpful discussions.

## **REFERENCES**

Awschalom, D. D.; Hanson, R.; Wrachtrup, J.; Zhou, B. B.
 Quantum Technologies with Optically Interfaced Solid-State

- Spins. Nat. Photonics 2018, 12, 516-527.
- (2) Anderson, C. P.; Bourassa, A.; Miao, K. C.; Wolfowicz, G.; Mintun, P. J.; Crook, A. L.; Abe, H.; Ul Hassan, J.; Son, N. T.; Ohshima, T.; Awschalom, D. D. Electrical and Optical Control of Single Spins Integrated in Scalable Semiconductor Devices. *Science* 2019, 366, 1225 LP – 1230.
- (3) Bourassa, A.; Anderson, C. P.; Miao, K. C.; Onizhuk, M.; Ma, H.; Crook, A. L.; Abe, H.; Ul-Hassan, J.; Ohshima, T.; Son, N. T.; Galli, G.; Awschalom, D. D. Entanglement and Control of Single Nuclear Spins in Isotopically Engineered Silicon Carbide. *Nat. Mater.* 2020, 19, 1319–1325.
- (4) Vandersypen, L. M. K.; Bluhm, H.; Clarke, J. S.; Dzurak, A. S.; Ishihara, R.; Morello, A.; Reilly, D. J.; Schreiber, L. R.; Veldhorst, M. Interfacing Spin Qubits in Quantum Dots and Donors—Hot, Dense, and Coherent. npj Quantum Inf. 2017, 3, 1–10.
- (5) Li, R.; Petit, L.; Franke, D. P.; Dehollain, J. P.; Helsen, J.; Steudtner, M.; Thomas, N. K.; Yoscovits, Z. R.; Singh, K. J.; Wehner, S.; Vandersypen, L. M. K.; Clarke, J. S.; Veldhorst, M. A Crossbar Network for Silicon Quantum Dot Qubits. Sci. Adv. 2018, 4, eaar3960.
- (6) Rose, B. C.; Huang, D.; Zhang, Z. H.; Tyryshkin, A. M.; Sangtawesin, S.; Srinivasan, S.; Loudin, L.; Markham, M. L.; Edmonds, A. M.; Twitchen, D. J.; Lyon, S. A.; de Leon, N. P. Observation of an Environmentally Insensitive Solid State Spin Defect in Diamond. Science 2018, 361, 60-63.
- Davis, E. J.; Bentsen, G.; Homeier, L.; Li, T.; Schleier-Smith, M.
  H. Photon-Mediated Spin-Exchange Dynamics of Spin-1 Atoms. Phys. Rev. Lett. 2019, 122, 10405.
- (8) Atzori, M.; Sessoli, R. The Second Quantum Revolution: Role and Challenges of Molecular Chemistry. J. Am. Chem. Soc. 2019, 141, 11339–11352.
- (9) Kjaergaard, M.; Schwartz, M. E.; Braumüller, J.; Krantz, P.; Wang, J. I. J.; Gustavsson, S.; Oliver, W. D. Superconducting Qubits: Current State of Play. *Annu. Rev. Condens. Matter Phys.* 2020, 11, 369–395.
- (10) Ferrenti, A. M.; de Leon, N. P.; Thompson, J. D.; Cava, R. J. Identifying Candidate Hosts for Quantum Defects via Data Mining. npj Comput. Mater. 2020, 6, 2-7.
- (11) Harris, I.; Ciccarino, C. J.; Flick, J.; Englund, D. R.; Narang, P. Group-III Quantum Defects in Diamond Are Stable Spin-1 Color Centers. Phys. Rev. B 2020, 102, 195206.
- (12) Zhong, H. Sen; Wang, H.; Deng, Y. H.; Chen, M. C.; Peng, L. C.; Luo, Y. H.; Qin, J.; Wu, D.; Ding, X.; Hu, Y.; Hu, P.; Yang, X. Y.; Zhang, W. J.; Li, H.; Li, Y.; Jiang, X.; Gan, L.; Yang, G.; You, L.; Wang, Z.; Li, L.; Liu, N. Le; Lu, C. Y.; Pan, J. W. Quantum Computational Advantage Using Photons. *Science* **2020**, *370*, 1460–1463.
- (13) Lovchinsky, I.; Sushkov, A. O.; Urbach, E.; de Leon, N. P.; Choi, S.; De Greve, K.; Evans, R.; Gertner, R.; Bersin, E.; Müller, C.; McGuinness, L.; Jelezko, F.; Walsworth, R. L.; Park, H.; Lukin, M. D. Nuclear Magnetic Resonance Detection and Spectroscopy of Single Proteins Using Quantum Logic. Science 2016, 351, 836 LP 841.
- (14) Hensen, B.; Bernien, H.; Dreaú, A. E.; Reiserer, A.; Kalb, N.; Blok, M. S.; Ruitenberg, J.; Vermeulen, R. F. L.; Schouten, R. N.; Abellán, C.; Amaya, W.; Pruneri, V.; Mitchell, M. W.; Markham, M.; Twitchen, D. J.; Elkouss, D.; Wehner, S.; Taminiau, T. H.; Hanson, R. Loophole-Free Bell Inequality Violation Using Electron Spins Separated by 1.3 Kilometres. *Nature* 2015, 526, 682–686.
- (15) Barry, J. F.; Turner, M. J.; Schloss, J. M.; Glenn, D. R.; Song, Y.; Lukin, M. D.; Park, H.; Walsworth, R. L. Optical Magnetic Detection of Single-Neuron Action Potentials Using Quantum Defects in Diamond. *Proc. Natl. Acad. Sci. U. S. A.* 2016, 113, 14133–14138.
- (16) Heremans, F. J.; Yale, C. G.; Awschalom, D. D. Control of Spin Defects in Wide-Bandgap Semiconductors for Quantum Technologies. Proc. IEEE 2016, 104, 2009–2023.
- (17) Doherty, M. W.; Manson, N. B.; Delaney, P.; Jelezko, F.; Wrachtrup, J.; Hollenberg, L. C. L. The Nitrogen-Vacancy Colour Centre in Diamond. *Phys. Rep.* 2013, 528, 1–45.
- (18) Christle, D. J.; Falk, A. L.; Andrich, P.; Klimov, P. V.; Hassan, J. U.; Son, N. T.; Janzén, E.; Ohshima, T.; Awschalom, D. D. Isolated Electron Spins in Silicon Carbide with Millisecond

- Coherence Times. Nat. Mater. 2015, 14, 160-163.
- (19) Koehl, W. F.; Diler, B.; Whiteley, S. J.; Bourassa, A.; Son, N. T.; Janzén, E.; Awschalom, D. D. Resonant Optical Spectroscopy and Coherent Control of Cr<sup>4+</sup> Spin Ensembles in SiC and GaN. *Phys. Rev. B* 2017, 95.
- (20) Chen, S.; Raha, M.; Phenicie, C. M.; Ourari, S.; Thompson, J. D. Parallel Single-Shot Measurement and Coherent Control of Solid-State Spins below the Diffraction Limit. *Science* 2020, 370, 592–595.
- (21) Siyushev, P.; Xia, K.; Reuter, R.; Jamali, M.; Zhao, N.; Yang, N.; Duan, C.; Kukharchyk, N.; Wieck, A. D.; Kolesov, R.; Wrachtrup, J. Coherent Properties of Single Rare-Earth Spin Qubits. *Nat. Commun.* 2014, 5, 1–6.
- (22) DiVincenzo, D. P. The Physical Implementation of Quantum Computation. Fortschritte der Phys. 2000, 48, 771–783.
- (23) Degen, C. L.; Reinhard, F.; Cappellaro, P. Quantum Sensing. *Rev. Mod. Phys.* **2017**, *89*, 1–39.
- (24) Yamabayashi, T.; Atzori, M.; Tesi, L.; Cosquer, G.; Santanni, F.; Boulon, M. E.; Morra, E.; Benci, S.; Torre, R.; Chiesa, M.; Sorace, L.; Sessoli, R.; Yamashita, M. Scaling Up Electronic Spin Qubits into a Three-Dimensional Metal-Organic Framework. J. Am. Chem. Soc. 2018, 140, 12090–12101.
- (25) Ariciu, A. M.; Woen, D. H.; Huh, D. N.; Nodaraki, L. E.; Kostopoulos, A. K.; Goodwin, C. A. P.; Chilton, N. F.; McInnes, E. J. L.; Winpenny, R. E. P.; Evans, W. J.; Tuna, F. Engineering Electronic Structure to Prolong Relaxation Times in Molecular Qubits by Minimising Orbital Angular Momentum. Nat. Commun. 2019, 10, 1–8.
- (26) Cimatti, I.; Bondì, L.; Serrano, G.; Malavolti, L.; Cortigiani, B.; Velez-Fort, E.; Betto, D.; Ouerghi, A.; Brookes, N. B.; Loth, S.; Mannini, M.; Totti, F.; Sessoli, R. Vanadyl Phthalocyanines on Graphene/SiC(0001): Toward a Hybrid Architecture for Molecular Spin Qubits. Nanoscale Horizons 2019, 4, 1202–1210.
- (27) Thiele, S.; Balestro, F.; Ballou, R.; Klyatskaya, S.; Ruben, M.; Wernsdorfer, W. Electrically Driven Nuclear Spin Resonance in Single-Molecule Magnets. *Science* 2014.
- (28) Zadrozny, J. M.; Gallagher, A. T.; Harris, T. D.; Freedman, D. E. A Porous Array of Clock Qubits. J. Am. Chem. Soc. 2017, 139, 7089–7094.
- (29) Yu, C. J.; Krzyaniak, M. D.; Fataftah, M. S.; Wasielewski, M. R.; Freedman, D. E. A Concentrated Array of Copper Porphyrin Candidate Qubits. *Chem. Sci.* 2019, 10, 1702–1708.
- (30) Fataftah, M. S.; Krzyaniak, M. D.; Vlaisavljevich, B.; Wasielewski, M. R.; Zadrozny, J. M.; Freedman, D. E. Metal-Ligand Covalency Enables Room Temperature Molecular Qubit Candidates. Chem. Sci. 2019, 10, 6707–6714.
- (31) Jackson, C. E.; Lin, C. Y.; Johnson, S. H.; Van Tol, J.; Zadrozny, J. M. Nuclear-Spin-Pattern Control of Electron-Spin Dynamics in a Series of V(Iv) Complexes. *Chem. Sci.* 2019, 10, 8447– 8454.
- (32) Graham, M. J.; Yu, C. J.; Krzyaniak, M. D.; Wasielewski, M. R.; Freedman, D. E. Synthetic Approach To Determine the Effect of Nuclear Spin Distance on Electronic Spin Decoherence. J. Am. Chem. Soc. 2017, 139, 3196–3201.
- Yu, C. J.; Graham, M. J.; Zadrozny, J. M.; Niklas, J.; Krzyaniak, M. D.; Wasielewski, M. R.; Poluektov, O. G.; Freedman, D. E. Long Coherence Times in Nuclear Spin-Free Vanadyl Qubits. J. Am. Chem. Soc. 2016, 138, 14678–14685.
- (34) Bayliss, S. L.; Laorenza, D. W.; Mintun, P. J.; Diler, B.; Freedman, D. E.; Awschalom, D. D. Optically Addressable Molecular Spins for Quantum Information Processing. *Science* 2020, 370, 1309–1312.
- (35) Fataftah, M. S.; Freedman, D. E. Progress towards Creating Optically Addressable Molecular Qubits. *Chem. Commun.* 2018, 54, 13773–13781.
- (36) Fataftah, M. S.; Bayliss, S. L.; Laorenza, D. W.; Wang, X.; Phelan, B. T.; Wilson, C. B.; Mintun, P. J.; Kovos, B. D.; Wasielewski, M. R.; Han, S.; Sherwin, M. S.; Awschalom, D. D.; Freedman, D. E. Trigonal Bipyramidal V³+Complex as an Optically Addressable Molecular Qubit Candidate. J. Am. Chem. Soc. 2020, 142, 20400–20408.
- (37) Wojnar, M. K.; Laorenza, D. W.; Schaller, R. D.; Freedman, D. E. Nickel(II) Metal Complexes as Optically Addressable Qubit

- Candidates. J. Am. Chem. Soc. 2020, 142, 14826.
- (38) Krzystek, J.; Park, J. H.; Meisel, M. W.; Hitchma, M. A.; Stratemeier, H.; Brunel, L. C.; Telser, J. EPR Spectra from "EPR-Silent" Species: High-Frequency and High-Field EPR Spectroscopy of Pseudotetrahedral Complexes of Nickel(II). Inorg. Chem. 2002, 41, 4478–4487.
- (39) Krzystek, J.; Ozarowski, A.; Telser, J.; Crans, D. C. High-Frequency and -Field Electron Paramagnetic Resonance of Vanadium(IV, III, and II) Complexes. *Coord. Chem. Rev.* **2015**, 301–302, 123–133.
- (40) Mowat, W.; Shortland, A.; Yagupsky, G.; Hill, N. J.; Yagupsky, M.; Wilkinson, G. Elimination Stabilized Alkyls. Part I. Chromium, Molybdenum, Tungsten, and Vanadium. J. Chem. Soc. Dalt. Trans. 1972, 533–542.
- (41) Mowat, W.; Shortland, A. J.; Hill, N. J.; Wilkinson, G. Elimination Stabilized Alkyls. Part II. Neopentyl and Related Alkyls of Chromium(IV). J. Chem. Soc. Dalt. Trans. 1972, 770–778.
- (42) Bucinsky, L.; Breza, M.; Malček, M.; Powers, D. C.; Hwang, S. J.; Krzystek, J.; Nocera, D. G.; Telser, J. High-Frequency and -Field EPR (HFEPR) Investigation of a Pseudotetrahedral Cr<sup>IV</sup> Siloxide Complex and Computational Studies of Related Cr<sup>IV</sup>L<sub>4</sub> Systems. *Inorg. Chem.* 2019, 58, 4907–4920.
- (43) Reichenauer, F.; Wang, C.; Förster, C.; Boden, P.; Ugur, N.; Báez-Cruz, R.; Kalmbach, J.; Carrella, L. M.; Rentschler, E.; Ramanan, C.; Niedner-Schatteburg, G.; Gerhards, M.; Seitz, M.; Resch-Genger, U.; Heinze, K. Strongly Red-Emissive Molecular Ruby [Cr(Bpmp)<sub>2</sub>]<sup>3+</sup> Surpasses [Ru(Bpy)<sub>3</sub>]<sup>2+</sup>. J. Am. Chem. Soc. **2021**, *143*, 11843–11855.
- (44) Joyce, J. P.; Portillo, R. I.; Nite, C. M.; Nite, J. M.; Nguyen, M. P.; Rappé, A. K.; Shores, M. P. Electronic Structures of Cr(III) and V(II) Polypyridyl Systems: Undertones in an Isoelectronic Analogy. *Inorg. Chem.* 2021.
- (45) Koschmieder, S. U.; McGilligan, B. S.; McDermott, G.; Arnold, J.; Wilkinson, G.; Hussain-Bates, B.; Hursthouse, M. B. Aryl and Aryne Complexes of Chromium, Molybdenum, and Tungsten. X-Ray Crystal Structures of [Cr(2-MeC6H4)(μ-2-MeC6H4)(PMe3)]2, Mo(H2-2-MeC6H3)(2-MeC6H4)2(PMe2Ph)2, and W(H2-2,5-Me2C6H2)(2,5-Me2C6H3)2-(PMe3)2. J. Chem. Soc. Dalt. Trans. 1990, No. 11, 3427–3433.
- (46) Schulzke, C.; Enright, D.; Sugiyama, H.; LeBlanc, G.; Gambarotta, S.; Yap, G. P. A.; Thompson, L. K.; Wilson, D. R.; Duchateau, R. The Unusual Stability of Homoleptic Di- and Tetravalent Chromium Alkyls. *Organometallics* 2002, 21, 3810–3816.
- (47) Stavropoulos, P.; Savage, P. D.; Tooze, R. P.; Wilkinson, G.; Hussain, B.; Motevalli, M.; Hursthouse, M. B. The Synthesis and X-Ray Crystal Structures of Homoleptic Tetrahedral Aryls of Osmium(IV) and of Cyclohexyls of Ruthenium(IV), Osmium(IV), and Chromium(IV). J. Chem. Soc. Dalt. Trans. 1987. 2. 557–562.
- (48) Basi, J. S.; Bradley, D. C.; Chisholm, M. H. Covalent Compounds of Quadrivalent Transition Metals. Part III. Chromium(IV) Dialkylamides. J. Chem. Soc. A 1971, 1433–1436.
- (49) Gramlich, V.; Pfefferkorn, K. The Crystal Structure of Tetrakis(2-Methyl-2-Phenyl-Propyl)Chromium. *J. Organomet. Chem.* **1973**, *61*, 247–248.
- (50) Cardin, C. J.; Cardin, D. J.; Roy, A. Synthesis and X-Ray Crystal and Molecular Structure of Tetrakis(2,2-Dimethyl-1-Phenylethenyl)Chromium(IV), the First Structurally-Characterised Homoleptic Alkenyl Compound of a Transition Metal. J. Chem. Soc. Chem. Commun. 1978, 899–900.
- (51) Alonso, P. J.; Forniés, J.; García-Monforte, M. A.; Martín, A.; Menjón, B.; Rillo, C. Synthesis and Characterization of New Paramagnetic Tetraaryl Derivatives of Chromium and Molybdenum. J. Organomet. Chem. 2007, 692, 3236–3247.
- (52) Alonso, P. J.; Fornies, J.; Garcia-Monforte, M. A.; Martin, A.; Menjon, B. New Homoleptic Organometallic Derivatives of Vanadium(III) and Vanadium(IV): Synthesis, Characterization, and Study of Their Electrochemical Behaviour. Chem Eur. J. 2005, 11, 4713.
- (53) Figgis N., B.; Hitchman A., M. *Ligand Field Theory and Its Applications*; Wiley-VCH: New York, 2000.
- (54) Park, K.; Novotny, M. A.; Dalal, N. S.; Hill, S.; Rikvold, P. A.

- Effects of D-Strain, g-Strain, and Dipolar Interactions on EPR Linewidths of the Molecular Magnets  $Fe_8$  and  $Mn_{12}$ . *Phys. Rev. B* **2001**, *65*, 14426.
- (55) Ward, G. A.; Bower, B. K.; Findlay, M.; Chien, J. C. W. Electron Paramagnetic Resonance of Tetrakis(1-Norbonyl)Chromium. *Inorg. Chem.* 1974, 13, 614–617.
- (56) Eaton, S. S.; Harbridge, J. .; Rinard, G. A.; Eaton, G. R.; Weber, R.
  T. Frequency Dependence of Electron Spin Relaxation for Three S = 1/2 Species Doped into Diamagnetic Solid Hosts.
  Appl. Magn. Reson. 2001, 20, 151–157.
- (57) Chen, H.; Maryasov, A. G.; Rogozhnikova, O. Y.; Trukhin, D. V.; Tormyshev, V. M.; Bowman, M. K. Electron Spin Dynamics and Spin-Lattice Relaxation of Trityl Radicals in Frozen Solutions. *Phys. Chem. Chem. Phys.* 2016, 18, 24954–24965.
- (58) Atsarkin, V. A. On the Mechanism of Paramagnetic Relaxation. Sov. Phys. – JETP **1966**, 22, 106–113.
- (59) Harris, E. A.; Yngvesson, K. S. Spin-Lattice Relaxation in Some Iridium Salts II. Relaxation of Nearest-Neighbour Exchange-Coupled Pairs. J. Phys. C Solid State Phys. 1968, 1, 1011–1023.
- (60) Harris, E. A. Cross-Relaxation between Single Ions and Exchange-Coupled Clusters. J. Phys. C Solid State Phys. 1969, 2, 1413–1415.
- (61) Bates, C. A.; Steggles, P.; Vasson, A.; Bates, C. A.; Bates, C. A.; Vasson, A. Non-Resonant Cross-Relaxation and Its Occurrence in Vanadium-Doped Rubies. J. Phys. C Solid State Phys. 1976, 9, 2413–2427.
- (62) Escalera-Moreno, L.; Suaud, N.; Gaita-Ariño, A.; Coronado, E. Determining Key Local Vibrations in the Relaxation of Molecular Spin Qubits and Single-Molecule Magnets. J. Phys. Chem. Lett. 2017, 8, 1695–1700.
- (63) Atzori, M.; Benci, S.; Morra, E.; Tesi, L.; Chiesa, M.; Torre, R.; Sorace, L.; Sessoli, R. Structural Effects on the Spin Dynamics of Potential Molecular Qubits. *Inorg. Chem.* 2018, 57, 731– 740
- (64) Escalera-Moreno, L.; Baldoví, J. J.; Gaita-Ariño, A.; Coronado, E. Spin States, Vibrations and Spin Relaxation in Molecular Nanomagnets and Spin Qubits: A Critical Perspective. *Chem. Sci.* 2018, 9, 3265–3275.
- (65) Du, J. -L; More, K. M.; Eaton, S. S.; Eaton, G. R. Orientation Dependence of Electron Spin Phase Memory Relaxation Times in Copper(II) and Vanadyl Complexes in Frozen Solution. Isr. J. Chem. 1992, 32, 351–355.
- (66) Jackson, C. E.; Lin, C. Y.; van Tol, J.; Zadrozny, J. M. Orientation Dependence of Phase Memory Relaxation in the V(IV) Ion at High Frequencies. Chem. Phys. Lett. 2020, 739, 137034.
- (67) Stanwix, P. L.; Pham, L. M.; Maze, J. R.; Le Sage, D.; Yeung, T. K.; Cappellaro, P.; Hemmer, P. R.; Yacoby, A.; Lukin, M. D.; Walsworth, R. L. Coherence of Nitrogen-Vacancy Electronic Spin Ensembles in Diamond. *Phys. Rev. B Condens. Matter Mater. Phys.* 2010, 82, 7–10.
- (68) Hong, S.; Grinolds, M. S.; Pham, L. M.; Le Sage, D.; Luan, L.; Walsworth, R. L.; Yacoby, A. Nanoscale Magnetometry with NV Centers in Diamond. MRS Bull. 2013, 38, 155–161.
- (69) Clevenson, H.; Trusheim, M. E.; Teale, C.; Schröder, T.; Braje, D.; Englund, D. Broadband Magnetometry and Temperature Sensing with a Light-Trapping Diamond Waveguide. *Nat. Phys.* 2015, 11, 393–397.
- (70) Lee, S. Y.; Niethammer, M.; Wrachtrup, J. Vector Magnetometry Based on S= 3/2 Electronic Spins. Phys. Rev. B - Condens. Matter Mater. Phys. 2015, 92, 1–7.
- (71) Qiu, Z.; Vool, U.; Hamo, A.; Yacoby, A. Nuclear Spin Assisted Magnetic Field Angle Sensing. npj Quantum Inf. 2021, 7, 1–7.
- (72) Sinha, M.; Pearson, T. J.; Reeder, T. R.; Vivanco, H. K.; Freedman, D. E.; Phelan, W. A.; McQueen, T. M. Introduction of Spin Centers in Single Crystals of Ba<sub>2</sub>CaWO<sub>6-δ</sub>. *Phys. Rev. Mater.* **2019**, *3*, 125002.
- (73) Whangbo, M. H.; Gordon, E. E.; Xia Lee, C. Prediction of Spin Orientations in Terms of HOMO-LUMO Interactions Using Spin-Orbit Coupling as Perturbation. Acc. Chem. Res. 2015, 48, 3080-3087.
- (74) Rohrer, M.; Gast, P.; Möbius, K.; Prisner, T. F. Anisotropic Motion of Semiquinones in Photosynthetic Reaction Centers of Rhodobacter Sphaeroides R26 and in Frozen Isopropanol Solution as Measured by Pulsed High-Field EPR at 95 GHz.

- Chem. Phys. Lett. 1996, 259, 523-530.
- (75) Atherton, N. M. Principles of Electron Spin Resonance; Horwood, E., Kemp, T. J., Eds.; Ellis Horwood Limited: West Sussex, England, 1993.
- (76) Kohn, W.; Sham, L. J. Self-Consistent Equations Including Exchange and Correlation Effects. Phys. Rev. 1965, 140, A1133-A1138.
- (77) Pople, J. A.; Gill, P. M. W.; Handy, N. C. Spin-unrestricted Character of Kohn-Sham Orbitals for Open-shell Systems. *Int. J. Quantum Chem.* 1995, 56, 303–305.
- (78) Lee, C.; Yang, W.; Parr, R. G. Development of the Colle-Salvetti Correlation-Energy Formula into a Functional of the Electron Density. Phys. Rev. B 1988, 37, 785–789.
- (79) Becke, A. D. Density-Functional Thermochemistry. III. The Role of Exact Exchange. J. Chem. Phys. 1993, 98, 5648–5652.
- (80) Weigend, F.; Ahlrichs, R. Balanced Basis Sets of Split Valence, Triple Zeta Valence and Quadruple Zeta Valence Quality for H to Rn: Design and Assessment of Accuracy. Phys. Chem. Chem. Phys. 2005, 7, 3297–3305.
- (81) Weigend, F. Accurate Coulomb-Fitting Basis Sets for H to Rn. Phys. Chem. Chem. Phys. 2006, 8, 1057–1065.
- (82) Neese, F.; Wennmohs, F.; Hansen, A.; Becker, U. Efficient, Approximate and Parallel Hartree-Fock and Hybrid DFT Calculations. A "chain-of-Spheres" Algorithm for the Hartree-Fock Exchange. Chem. Phys. 2009, 356, 98–109.
- (83) Grimme, S.; Ehrlich, S.; Goerigk, L. Effect of the Damping Function in Dispersion Corrected Density Functional Theory. J. Comput. Chem. 2011, 32, 1456–1465.
- (84) Neese, F. An Improvement of the Resolution of the Identity Approximation for the Formation of the Coulomb Matrix. J. Comput. Chem. 2003, 24, 1740–1747.
- (85) Grimme, S.; Antony, J.; Ehrlich, S.; Krieg, H. A Consistent and Accurate Ab Initio Parametrization of Density Functional Dispersion Correction (DFT-D) for the 94 Elements H-Pu. J. Chem. Phys. 2010, 132, 154104.
- (86) Neese, F. The ORCA Program System. WIREs Comput. Mol. Sci. 2012. 2. 73–78.
- (87) Runge, E.; Gross, E. K. U. Density-Functional Theory for Time-Dependent Systems. Phys. Rev. Lett. 1984, 52, 997–1000.
- (88) Dreuw, A.; Head-Gordon, M. Single-Reference Ab Initio Methods for the Calculation of Excited States of Large Molecules. Chem. Rev. 2005. 105, 4009-4037.
- (89) Neese, F. Prediction of Molecular Properties and Molecular Spectroscopy with Density Functional Theory: From Fundamental Theory to Exchange-Coupling. *Coord. Chem. Rev.* **2009**, *253*, 526–563.
- (90) Adamo, C.; Barone, V. Inexpensive and Accurate Predictions of Optical Excitations in Transition-Metal Complexes: The TDDFT/PBE0 Route. Theor. Chem. Acc. 2000, 105, 169–172.

- (91) Neese, F. A Critical Evaluation of DFT, Including Time-Dependent DFT, Applied to Bioinorganic Chemistry. J. Biol. Inorg. Chem. 2006, 11, 702–711.
- (92) Martin, R. L. Natural Transition Orbitals. J. Chem. Phys. 2003, 118, 4775–4777.
- (93) Otto, S.; Dorn, M.; Förster, C.; Bauer, M.; Seitz, M.; Heinze, K. Understanding and Exploiting Long-Lived near-Infrared Emission of a Molecular Ruby. Coord. Chem. Rev. 2018, 359, 102–111.
- (94) Förster, C.; Heinze, K. Photophysics and Photochemistry with Earth-Abundant Metals-Fundamentals and Concepts. *Chem. Soc. Rev.* 2020, 49, 1057–1070.
- (95) Dorn, M.; Kalmbach, J.; Boden, P.; Päpcke, A.; Gómez, S.; Förster, C.; Kuczelinis, F.; Carrella, L. M.; Büldt, L. A.; Bings, N. H.; Rentschler, E.; Lochbrunner, S.; González, L.; Gerhards, M.; Seitz, M.; Heinze, K. A Vanadium(III) Complex with Blue and NIR-II Spin-Flip Luminescence in Solution. J. Am. Chem. Soc. 2020, 142, 7947–7955.
- (96) Alyea, E. C.; Basi, J. S.; Bradley, D. C.; Chisholm, M. H. Covalent Compounds of Quadrivalent Transition Metals. Part II. Chromium(IV) Tertiary Alkoxides and Triethylsilyloxide. J. Chem. Soc. A 1971, 772–776.
- (97) Schrock, R. R.; Parshall, G. W. σ-Alkyl and -Aryl Complexes of the Group 4-7 Transition Metals. *Chem. Rev.* 1976, 76, 243– 268.
- (98) Alonso, P. J.; Forniés, J.; García-Monforte, M. A.; Martín, A.; Menjón, B.; Rillo, C. A New Series of Homoleptic, Paramagnetic Organochromium Derivatives: Synthesis, Characterization, and Study of Their Magnetic Properties. *Chem. - A Eur. J.* 2002, 8, 4056–4065.
- (99) Mirzoyan, R.; Hadt, R. G. The Dynamic Ligand Field of a Molecular Qubit: Decoherence through Spin-Phonon Coupling. Phys. Chem. Chem. Phys. 2020, 22, 11249–11265.
- (100) Mirzoyan, R.; Kazmierczak, N. P.; Hadt, R. G. Deconvolving Contributions to Decoherence in Molecular Electron Spin Qubits: A Dynamic Ligand Field Approach. Chem. – A Eur. J. 2021, 1–14.
- (101) Smith, A. M.; Mancini, M. C.; Nie, S. Bioimaging: Second Window for in Vivo Imaging. *Nat. Nanotechnol.* **2009**, *4*, 710–711
- (102) Vanquickenborne, L. G.; Haspeslagh, L. On the Meaning of Spin-Pairing Energy in Transition-Metal Ions. *Inorg. Chem.* 1982, 21, 2448–2454.
- (103) Bower, B. K.; Tennent, H. G. Transition Metal Bicyclo[2.2.1]Hept-l-Yls. J. Am. Chem. Soc. **1972**, 94, 2512– 2514.

